Research Article | Vol. 4, No. 12 / December 2017 / Optica 1498

optica

Single-chip, mid-infrared array for room temperature video rate imaging

Chengzhi Xie,[1,*] Mohsin Aziz,[1,2] Vincenzo Pusino,[1] Ata Khalid,[3] Matthew Steer,[1] Iain G. Thayne,[1] Marc Sorel,[1] and David R. S. Cumming[1]

[1]School of Engineering, University of Glasgow, Glasgow G128QQ, UK
[2]School of Physics & Astronomy, University of Southampton, Southampton SO171BJ, UK
[3]Centre for Electronic Warfare Information and Cyber, Cranfield University, Shrivenham SN68LA, UK
*Corresponding author: chengzhi.xie@glasgow.ac.uk

Received 3 August 2017; revised 29 October 2017; accepted 31 October 2017 (Doc. ID 304044); published 1 December 2017

The need for energy efficiency and lower emissions from industrial plants and infrastructures is driving research into novel sensor technologies, especially those that allow observing and measuring greenhouse gases, such as CO_2. CO_2 emissions can be captured using mid-infrared imagers, but at present, these are based on hybrid technologies that need expensive manufacturing and require cooling. The high price tag prevents a wider diffusion of mid-infrared imagers and hence their use for many low-cost and large-volume applications. Here we report a monolithic III-V technology that integrates GaAs transistors with an InSb photodiode array. The monolithic material system reduces costs and provides an excellent platform for the sensor system-on-chip. We present a focal plane array imaging technology operating at room temperature in the 3–6 μm wavelength range that will address the need for identification and measurement of a range of industrially important gases.

Published by The Optical Society under the terms of the Creative Commons Attribution 4.0 License. Further distribution of this work must maintain attribution to the author(s) and the published article's title, journal citation, and DOI.

OCIS codes: (040.1240) Arrays; (040.5160) Photodetectors; (040.3060) Infrared; (110.3080) Infrared imaging.

https://doi.org/10.1364/OPTICA.4.001498

1. INTRODUCTION

Many applications in numerous fields, from astronomy to defense and security, exploit medium-infrared (mid-IR) imagers [1]. Gas plume imaging is of particular interest in the wavelength range between 3 and 6 μm, a spectral region in which characteristic absorption lines of many gases lie (see Table 1).

Imaging of hydrocarbons is relevant to industrial asset management [3], and monitoring of greenhouse gases, such as carbon dioxide (CO_2) and methane (CH_4), has potential for environmental applications, such as visualization of plumes escaping from plant and storage wells [4]. However, several hurdles must be overcome for mid-IR imaging devices to become more widespread. An imaging device, such as a focal plane array (FPA), requires each pixel to be read individually. At visible wavelengths, silicon photodiodes (PDs), sensitive in the visible range, are monolithically integrated with silicon transistors to achieve individual pixel addressing [5]. However, established materials for mid-IR detection, such as indium antimonide (InSb) and mercury cadmium telluride (known as MCT), are well-suited for PDs [6,7], but transistors made on those substrates are not suitable for pixel addressing because they have high leakage currents [8,9]. Most commercially available imagers have remedied this problem by implementing the mid-IR PDs and the transistors for readout on separate chips. The PDs are usually fabricated on InSb or MCT material, while the readout integrated circuits (ROICs) are made on complementary metal oxide semiconductor (CMOS) silicon wafers. The III-V and silicon wafers are then diced into chips, and subsequently the silicon chip is flipped and connected to the InSb or MCT one through so-called indium bumps, a technique known as flip-chip bonding [10–12]. This hybridized approach does not allow wafer-level manufacturing and thus has high costs. A reliable monolithic approach capable of high temperature operation would significantly increase the yield of mid-IR imagers, reduce cost, and unlock applications outside of the limited defense and security markets.

Recently, antimonide-based detectors grown on GaAs demonstrated comparable performance to devices grown on more expensive InSb or GaSb materials [13,14,15]. The underlying GaAs provides a cost-saving substrate and also provides a functional layer for MEtal Semiconductor Field Effect Transistors (MESFETs). The MESFETs can then be used for active pixel addressing as part of an embedded multiplexer architecture. Following the first demonstration of an active InSb-based photopixel with a GaAs MESFET [16], we present the world's first, to the best of our knowledge, monolithic mid-IR imaging array based on on-chip integration of InSb PDs and GaAs readout circuits. The prototype arrays are fabricated as 4 × 4 and 8 × 8 pixel devices, and they allow room temperature image capturing in the

Table 1. Characteristic Absorption of Eight Gases in the 3–6 μm Range, Highlighting the Capabilities of Mid-IR Detectors When Used for Gas Sensing [2]

Gas	Typical Absorption (μm)
H_2O	3, 6
HCN	3.0
CH_4	3.3
NO_2	3.4
CH_2O	3.5
CO_2	4.2
N_2O	4.5
CO	4.7

mid-IR wavelength range. Moreover, the monolithic approach used has great flexibility since one can grow many other optically active layer structures on top of the GaAs transistor layers to create new III-V sensor system-on-chip components.

2. RESULTS

A. Device Structure and Functionality

Figure 1(a) shows a 3D schematic of a single pixel of the array device. From the image, the complexity of the structure is apparent; various growth and fabrication challenges (discussed together with the details of the experiments in Supplement 1) had to be overcome to complete the arrays. Each pixel is composed of an InSb PD connected in series with a GaAs MESFET. The GaAs MESFET is needed in order to control the access of each InSb PD to a shared read-line. The gate and drain of the MESFET are connected to a row addressing line and to a column read-line, respectively. The size of the InSb PD was chosen to be 150 μm × 150 μm, while

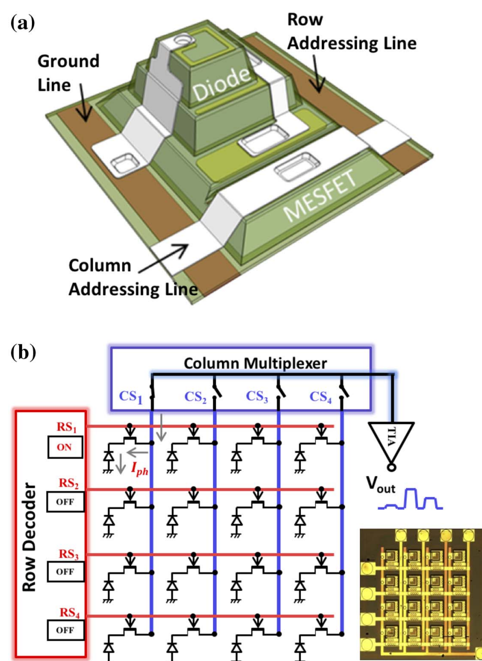

Fig. 1. (a) Diagram depicting the 3D pixel topography in the arrays: the schematic shows a single element of the FPA with the diode and MESFET fabricated side-by-side to achieve a completed pixel device. (b) The circuit diagram of the 4 × 4 array architecture illustrating the readout mechanism: the row decoder selects a row by switching its MESFETs to the ON state, so that the multiplexer can then read the photocurrent sequentially from each column.

the pixel pitch of the arrays was 400 μm, leading to a fill factor of approximately 14%. Maintaining the current pixel layout, the array pitch is easily scalable to 110 μm with a 25% fill factor. Changes to the epitaxial structure (e.g., merging the MESFET contact layer and the PD n-contact layer) can decrease the pitch further to approximately 50 μm and bring the fill factor to approximately 60%.

The circuit diagram of Fig. 1(b) illustrates the X–Y readout scheme chosen, enabling the array device (shown in the inset) to individually address the pixels and read the individual photocurrents. The chip was mounted and bonded to a ceramic leadless chip carrier. The chip carrier was then placed on a printed circuit board (PCB) where off-the-shelf multiplexers and decoders completed the data acquisition circuit. Previous work on a single PD and MESFET pair device demonstrated that when biased with a sufficiently low gate-source voltage, the MESFET was able to isolate completely the signal from the PD [16]. To address each individual pixel inside the array device, the row decoder switches the corresponding MESFETs to the ON state by applying a gate-source voltage of 0 V to select a row. Addressing is mutually exclusive. Hence, all the other MESFETs, in different rows, will be biased into the OFF state by applying a gate-source voltage of −5 V. Each column read-line is connected to a separate pad at the edge of the photodiode array chip. An off-chip multiplexer then reads the current of each column sequentially before the operation repeats for the next row. In this manner, every pixel's photocurrent is sequentially read, one-by-one. A transimpedance amplifier (TIA), also shown in Fig. 1(b), converts the photocurrent output sourced from each of the pixels into a voltage output. Note that, at the current stage, the readout circuit of Fig. 1(b) does not support charge storage at a pixel level. The photogenerated carriers are directly transferred out to the TIA when a certain pixel is addressed accordingly.

B. Electrical and Optical Characterization

The first step in the characterization of the monolithically hybridized arrays was to evaluate the photocurrent spectrum of each pixel with a Fourier transform infrared (FTIR) spectrometer. Figure 2 shows the photoresponse spectrum obtained from each of the pixels in the array. All pixels in the array have nearly identical characteristics, with their peak photoresponse at 4 μm showing 6% variation as compared to the average value. A uniform pixel response across the array is important for imaging applications since sensor-to-sensor variation will manifest itself in an image as fixed pattern noise. The pixels showed similar characteristics also in the absence of illumination, with an average dark current of 13 μA at near-zero bias and all pixels within 5% of this figure. When applying a small negative bias (−50 mV), the average dark current increased to 1.6 mA. In order to minimize the dark current, all devices were then measured with near-zero bias applied. Since experiments were carried out in standard atmosphere and at room temperature, we observed a sharp notch in each spectrum at 4.2 μm that is due to the absorption of light by atmospheric carbon dioxide. The dips in the spectra near 3 and 6 μm are due to absorption by water vapor in the laboratory's atmosphere.

In addition to using the FTIR to assess that each pixel in the array was responsive to mid-IR radiation, more experiments were carried out to determine several important detector figures of merit, including responsivity, quantum efficiency, noise

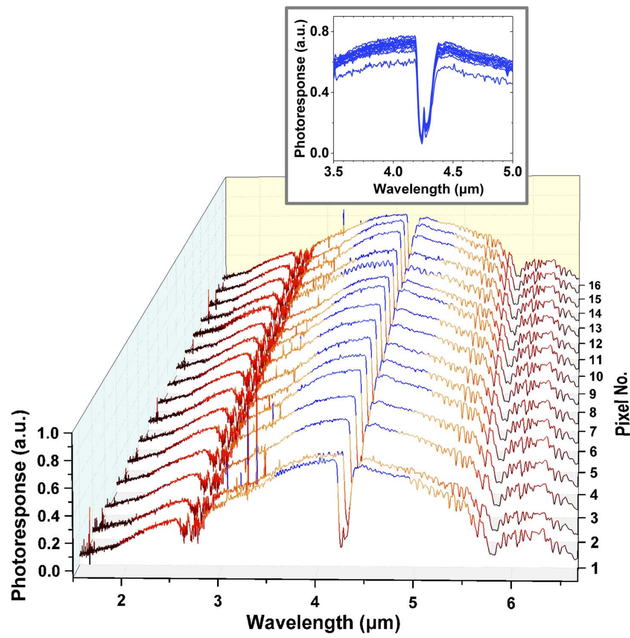

Fig. 2. Photoresponse spectra obtained using a FTIR spectrometer. Using the addressing architecture, we are able to show the individual spectra from each fabricated pixel in the 4×4 array. The inset shows the superposed peak photoresponse of all pixels.

equivalent power, and specific detectivity. Figure 3(a) shows the output signal obtained from the TIA as a function of the power illuminating the addressed pixel. We did not observe obvious nonlinearity in the system under any tested illumination condition. From the slope of the curve, a responsivity of approximately 5000 V/W at 4.57 µm was extracted. The extracted value corresponds to a source current, I_{pixel}, of 50 mA/W detected at the

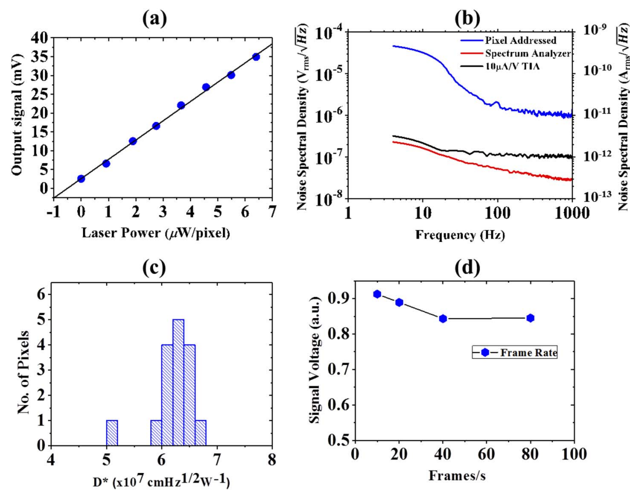

Fig. 3. (a) Responsivity of a typical pixel in the 4×4 array, with laser illumination at 4.57 µm. (b) A noise spectrum, measured with the RF analyzer without an input signal (red), with only the transimpedance amplifier connected to the analyzer (black), and finally with the amplified signal from the pixel connected to the input to the analyzer (blue). (c) A histogram comparing the specific detectivity of the 16 pixels in the 4×4 array. (d) The signal voltage dependence on the scanning speed, showing that an increase in the frame rate from 15 to 80 fps causes only a small signal loss.

amplifier input. The corresponding value of quantum efficiency, calculated using the active sensing area of the detector, was found to be 1.5%. Such a value might seem low compared to previously reported devices where the photocurrent signal in the photodiode was directly measured [17]. However, the quantum efficiency calculated here is an effective value for the whole circuit, which arises from the circuit chosen and also takes into account signal drop due to cointegrated switching transistors and the multiplexers. Since the array layout did not allow direct access to the PD contacts, we measured a single-pixel testing device, which has the same active sensing area as pixels inside the array devices. We found the quantum efficiency of the InSb PD itself was 28%. More details on signal loss and recovery methods are given in Supplement 1.

Noise measurements were performed by connecting the amplifier output to an RF spectrum analyzer. The noise response of the spectrum analyzer and of the transimpedance amplifier were both measured individually in order to isolate the noise contribution coming from the pixels themselves. Figure 3(b) shows all the curves obtained from the noise characterization. It can be seen that the dominant source of noise in the pixel at low frequencies is the $1/f$ noise, with a noise corner at approximately 100 Hz. The main source of noise is estimated to be the InSb PD, while the readout circuit has a negligible contribution to the total noise. The results of the noise characterization were used to extract the noise equivalent power (NEP) of the pixel, given by $\mathrm{NEP} = V_{\mathrm{noise(rms)}}/R_v$, where $V_{\mathrm{noise(rms)}}$ is the rms value of the noise, and R_v is the responsivity as previously defined, with illumination at a wavelength of 4.57 µm. For frequencies greater than 100 Hz, an NEP of $2.45 \times 10^{-10}\ \mathrm{W/Hz^{1/2}}$ was obtained. Using the measured NEP, the specific detectivity was obtained, given by $D^* = \sqrt{A}/\mathrm{NEP}$, where A is the active area of the pixel. A was 150×150 µm ($2.25 \times 10^{-8}\ \mathrm{m}^2$) in the 4×4 and 8×8 arrays. The NEP can also be used to calculate the noise equivalent irradiance (NEI), given by $\mathrm{NEI} = \mathrm{NEP}/A$. The NEI of the pixel is $0.011\ \mathrm{W/m^2}$. Figure 3(c) shows the distribution of the calculated D^* for all the pixels in the array. The distribution of D^* was found to have a median value of $6.12 \times 10^7\ \mathrm{cm\,Hz^{1/2}\,W^{-1}}$. Again, this value is an effective value that takes into account the signal loss introduced by the whole readout circuit, which includes the ON resistance of the multiplexer and the input impedance of the TIA. After de-embedding the data from the circuit, the D^* of the InSb photodiode itself is found to be approximately $2.7 \times 10^8\ \mathrm{cm\,Hz^{1/2}\,W^{-1}}$, which is comparable to the best results previously reported for antimonide devices [18–20] and also comparable to the typical performance of bolometric arrays at room temperature [21]. From the previous quantities we also derived the noise equivalent temperature difference (NETD), estimated to be from 1 to 10 K for a typical 300 K background scene (more details on the derivation of D^* and NETD are given in Supplement 1). All figures were obtained from room temperature measurements; applying thermoelectric cooling to the array is expected to boost the array performance by recovering the signal loss, reducing thermal noise in the PD, and allowing PD operation at a small negative bias.

The responsivity measurements discussed so far were carried out when scanning the 4×4 array at a rate of 15 frames per second (fps). The dependence of the signal level on the frame rate was also explored. Figure 3(d) shows the relative voltage signal measured at the amplifier output for several frame rates. The laser

power illuminating each pixel was kept constant at 6 μW throughout the experiment. It can be seen from Fig. 3(d) that with an increase of frame rate up to 40 and 80 fps (two values typically used for imagers), a small signal loss is observed. The integration time of our current array readout is given by $T_{\mathrm{int}} = 1/(\mathrm{FR} \cdot M \cdot N)$, where FR is the frame rate, M and N are the number of pixels in each row and column, respectively. At 80 fps, T_{int} is approximately 0.8 ms for the 4 × 4 array. For larger arrays (e.g., 64 × 64), and using a dedicated TIA for every column, the maximum FR achievable while keeping T_{int} at 0.8 ms would be approximately 20 fps. Ultimately, the maximum FR depends on the minimum T_{int} acceptable for the target application.

C. Video Rate Mid-IR Imaging Experiments

Obtaining images of an object with the fabricated arrays is the most direct way to demonstrate that the monolithically integrated GaAs-based readout circuits are scanning and extracting the photogenerated carriers from each pixel in the right sequence, with adequate sensitivity and low cross talk. For this purpose, the laser used to characterize the responsivity of the devices was used as a mid-IR source in an imaging experiment in which projected images of a mask were obtained.

Figure 4(a) illustrates the simplified experimental setup used for projection imaging. The QCL source that we used had a beam divergence of 30° horizontally and 70° vertically using the full width at half-maximum values. Owing to this characteristic, we did not attempt to collimate the beam. A CaF_2 lens (12.7 mm diameter, focal length $f = 20$ mm) was aligned and placed 40 mm away from the QCL source. A mask object—a piece

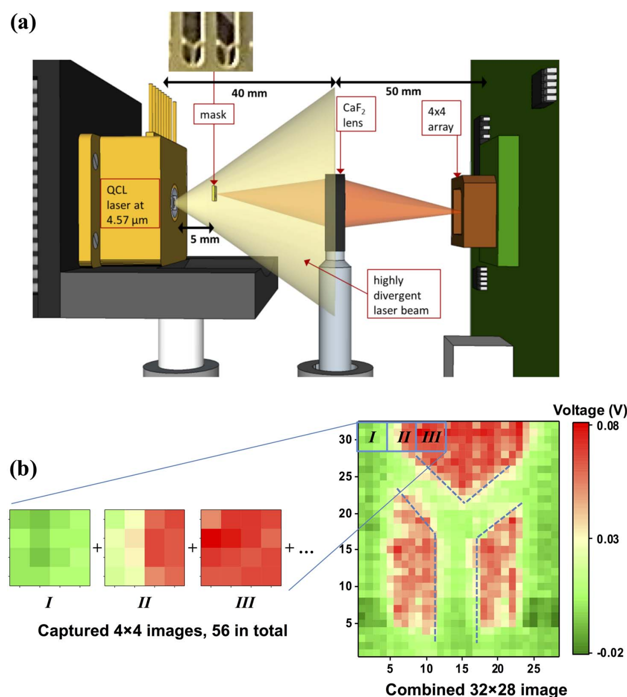

Fig. 4. (a) Schematic of the setup used to carry out imaging experiments. (b) An image of a patterned mask (shown in the figure) obtained by a combination of mechanical and electronic scanning using the 4 × 4 array. Subimages, including the examples I, II and III, captured electronically, are used to construct the full image.

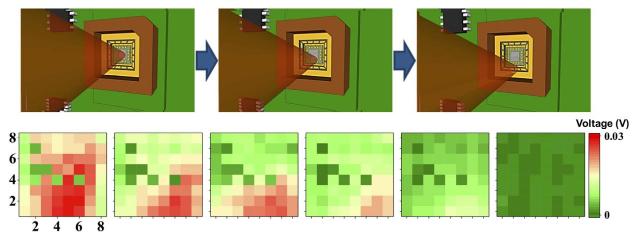

Fig. 5. Images of the FTIR glow bar source captured with the 8 × 8 pixel array. The images are taken in sequence, moving the array gradually across the globar spot.

of 200 μm thick brass with a Y-shaped pattern laser cut into it, was placed 5 mm away from the QCL source and thus at a distance $u = 35$ mm before the CaF_2 lens. The imaged object was attached to a XY translation stage to precisely control its movement [not shown in Fig. 4(a)]. The PCB where the 4 × 4 array fabricated in this work was mounted was placed beyond the lens, at a distance $v = 50$ mm, approximately corresponding to the plane where the image of the mask was expected to be formed according to the thin lens equation $(1/u + 1/v = 1/f)$.

As the pixel number of the prototype arrays was limited, to 4 × 4 in this case, only a small part of the mask shape could be imaged with a single image capture. In order to form a more complete image with higher resolution, the mask was mechanically scanned: every image capture with the 4 × 4 array was followed by a precise movement of the mask along either the X or Y direction before capturing a new image. Although imaging with a translational stage is also possible with a single detector, it is 16 times faster with a 4 × 4 array, and it is presented here mainly to prove the imaging potential of the technology once larger array formats are achieved. By using this scanning method, a 32 × 28 pixel image was obtained by combining 56 individually captured 4 × 4 images, as shown in Fig. 4(b). It can be seen that the composite image shows a clear Y-shaped pattern that matches the profile of the mask very well.

Further imaging experiments were also carried out to directly image the illumination pattern from the internal mid-IR source of the FTIR spectrometer at the instrument's emission port. This experiment was carried out using an 8×8 array, made in the same way as the 4 × 4 array, in order to have a larger sensing area and demonstrate imaging without mechanical scanning and image combination. As shown in Fig. 5, starting from a situation where the spot illuminated the center of the array, the device was moved gradually across the beam of mid-IR light. The obtained images show the detected scene gradually changing from bright to dark as the array is moved across the mid-IR illumination source.

3. CONCLUSIONS

In conclusion, mid-IR imaging using monolithically integrated antimonide-based arrays has been successfully demonstrated for the first time, to the best of our knowledge. The new technique, based on monolithic hybridization on a III-V semiconductor platform, has solved one of the main problems inhibiting widespread adoption of mid-IR imagers into mainstream medical, commercial, and industrial applications. Thanks to the hybridized growth method, transistor switches were implemented using GaAs layers. Further antimonide layers, grown on the same wafer, make it possible to achieve mid-IR image sensing. The novel wafer growth

and sensing-system-on-chip architecture presented in this paper is fully scalable to larger arrays, with a 64×64 market entry-level format easily achievable without changes in the technology. All imaging experiments were carried out at room temperature with predicted improvement of detection performance when a number of state-of-the-art structures, such as nBn barrier photodiodes, quantum well/dot detectors, and avalanche photodiodes, are integrated [22–25]. Many of these detectors are approaching background-limited performance under near room temperature (>200 K). Therefore, this array technology has great potential to provide a lower cost alternative compared to existing military, defense, and security technologies by eliminating the need for both flip-chip bonding and cooling. A compact, low-cost mid-IR imager will create opportunities in applications, such as asset management and safety in the oil and gas industries [26,27]. Affordable large-format mid-IR cameras will enable research exploration for the benefit of the medical and life sciences, where early results have shown promise for a new imaging modality for diagnosis and patient care [28,29].

Funding. Engineering and Physical Sciences Research Council (EPSRC) (EP/J018678/1, EP/M01326X/1).

Acknowledgment. The authors wish to thank all of the staff of the James Watt Nanofabrication Centre (JWNC) at the University of Glasgow for their assistance.

The dataset of the research is available at http://dx.doi.org/10.5525/gla.researchdata.554 [30].

See Supplement 1 for supporting content.

REFERENCES

1. A. Krier, *Mid-Infrared Semiconductor Optoelectronics* (Springer, 2006).
2. M. Vainio and L. Halonen, "Mid-infrared optical parametric oscillators and frequency combs for molecular spectroscopy," Phys. Chem. Chem. Phys. **18**, 4266–4294 (2016).
3. J. Sandsten, H. Edner, and S. Svanberg, "Gas visualization of industrial hydrocarbon emissions," Opt. Express **12**, 1443–1451 (2004).
4. H. Fabriol, A. Bitri, B. Bourgeois, M. Delatre, J. F. Girard, G. Pajot, and J. Rohmer, "Geophysical methods for CO_2 plume imaging: comparison of performances," Energy Procedia **4**, 3604–3611 (2011).
5. Y. Bai, J. Bajaj, J. W. Beletic, M. C. Farris, A. Joshi, S. Lauxtermann, A. Petersen, and G. Williams, "Teledyne imaging sensors: silicon CMOS imaging technologies for x-ray, UV, visible, and near infrared," Proc. SPIE **7021**, 702102 (2008).
6. T. Ashley, A. B. Dean, C. T. Elliott, C. F. McConville, G. J. Pryce, and C. R. Whitehouse, "Ambient temperature diodes and field-effect transistors in $InSb/In_{1-x}Al_xSb$," Appl. Phys. Lett. **59**, 1761–1763 (1991).
7. E. Theocharous and J. R. Birch, "Detectors for mid- and far-infrared spectrometry: selection and use," in *Handbook of Vibrational Spectroscopy*, J. M. Chalmers and P. R. Griffiths, eds. (Wiley, 2002), pp. 349–367.
8. S. Datta, T. Ashley, J. Brask, L. Buckle, M. Doczy, M. Emeny, D. Hayes, K. Hilton, R. Jefferies, T. Martin, T. J. Phillips, D. Wallis, P. Wilding, and R. Chau, "85 nm gate length enhancement and depletion mode InSb quantum well transistors for ultra-high speed and very low power digital logic applications," in *Electron Devices Meeting*, IEDM Technical Digest, December 5, 2005, pp. 763–766.
9. Y. Nemirovsky, S. Margalit, and I. Kidron, "n-channel insulated-gate field-effect transistors in $Hg_{1-x}Cd_xTe$ with $x = 0.215$," Appl. Phys. Lett. **36**, 466–468 (1980).
10. P. Capper and C. T. Elliott, eds., *Infrared Detectors and Emitters: Materials and Devices*, Electronic Materials Series (Springer, 2001), Vol. 8.
11. Y. Gau, L. Dai, S. Yang, P. Weng, K. Huang, Y. Liu, C. Chiang, J. Jih, Y. Cherng, and H. Chang, "256×256 InSb focal plane arrays," Proc. SPIE **4078**, 467–479 (2000).
12. H. Gupta, D. Samudraiah, M. Baghini, D. Sharma, A. Kumar, S. Chakrabarti, S. Paul, and R. Parmar, "Design of large dynamic range, low-power, high-precision ROIC for quantum dot infrared photodetector," Electron. Lett. **49**, 1018–1020 (2013).
13. A. Craig, C. Reyner, A. Marshall, and D. Huffaker, "Excess noise in GaAs and AlGaAs avalanche photodiodes with GaSb absorption regions—composite structures grown using interfacial misfit arrays," Appl. Phys. Lett. **104**, 213502 (2014).
14. E. Camargo, K. Ueno, Y. Kawakami, Y. Moriyasu, K. Nagase, M. Satou, H. Endo, K. Ishibashi, and N. Kuze, "Miniaturized InSb photovoltaic infrared sensor operating at room temperature," Opt. Eng. **47**, 014402 (2008).
15. E. Plis, J. Rodriguez, G. Balakrishnan, Y. Sharma, H. Kim, T. Rotter, and S. Krishna, "Mid-infrared InAs/GaSb strained layer superlattice detectors with nBn design grown on a GaAs substrate," Semicond. Sci. Technol. **25**, 085010 (2010).
16. C. Xie, V. Pusino, A. Khalid, M. J. Steer, M. Sorel, I. G. Thayne, and D. R. S. Cumming, "Monolithic integration of an active InSb-based mid-infrared photo-pixel with a GaAs MESFET," IEEE Trans. Electron Devices **62**, 4069–4075 (2015).
17. V. Pusino, C. Xie, A. Khalid, I. G. Thayne, and D. R. S. Cumming, "InSb photodiodes for monolithic active focal plane arrays on GaAs substrates," IEEE Trans. Electron Devices **63**, 3135–3142 (2016).
18. K. Ueno, E. G. Camargo, T. Katsumata, H. Goto, N. Kuze, Y. Kangawa, and K. Kakimoto, "InSb mid-infrared photon detector for room-temperature operation," Jpn. J. Appl. Phys. **52**, 092202 (2013).
19. G. R. Nash, H. L. Forman, S. J. Smith, P. B. Robinson, L. Buckle, S. D. Coomber, M. T. Emeny, N. T. Gordon, and T. Ashley, "Mid-infrared AlxIn1-xSb light-emitting diodes and photodiodes for hydrocarbon sensing," IEEE Sens. J. **9**, 1240–1243 (2009).
20. I. Kimukin, N. Biyikli, and E. Ozbay, "InSb high-speed photodetectors grown on GaAs substrate," J. Appl. Phys. **94**, 5414–5416 (2003).
21. R. Bhan, R. Saxena, C. Jalwani, and S. Lomash, "Uncooled infrared microbolometer arrays and their characterisation techniques," Def. Sci. J. **59**, 580–589 (2009).
22. A. Craig, A. Marshall, Z.-B. Tian, S. Krishna, and A. Krier, "Mid-infrared $InAs_{0.79}Sb_{0.21}$-based nBn photodetectors with $Al_{0.9}Ga_{0.2}As_{0.1}Sb_{0.9}$ barrier layers, and comparisons with $InAs_{0.87}Sb_{0.13}$ p-i-n diodes, both grown on GaAs using interfacial misfit arrays," Appl. Phys. Lett. **103**, 253502 (2013).
23. A. Rogalski, P. Martyniuk, and M. Kopytko, "InAs/GaSb type-II superlattice infrared detectors: future prospect," Appl. Phys. Rev. **4**, 031304 (2017).
24. Z. Tian and S. Krishna, "Mid-infrared metamorphic interband cascade photodetectors on GaAs substrates," Appl. Phys. Lett. **107**, 211114 (2015).
25. M. Zavvari, "Quantum-dot-based single-photon avalanche detector for mid-infrared applications," J. Opt. Soc. Am. B **32**, 737–742 (2015).
26. W. Ye, C. Li, C. Zheng, N. P. Sanchez, A. K. Gluszek, A. J. Hudzikowski, L. Dong, R. J. Griffin, and F. K. Tittel, "Mid-infrared dual-gas sensor for simultaneous detection of methane and ethane using a single continuous-wave interband cascade laser," Opt. Express **24**, 16973–16985 (2016).
27. L. Tao, K. Sun, M. Amir Khan, D. J. Miller, and M. A. Zondlo, "Compact and portable open-path sensor for simultaneous measurements of atmospheric N_2O and CO using a quantum cascade laser," Opt. Express **20**, 28106–28118 (2012).
28. R. K. Saku and S. Mordechai, "Fourier transform infrared spectroscopy in cancer detection," Future Oncol. **1**, 635–647 (2005).
29. B. R. Wood, K. R. Bambery, M. W. A. Dixon, L. Tilley, M. J. Nasse, E. Mattson, and C. J. Hirschmugl, "Diagnosing malaria infected cells at the single level using focal plane array Fourier transform infrared imaging spectroscopy," Analyst **139**, 4769–4774 (2014).
30. The dataset of the research is available at http://dx.doi.org/10.5525/gla.researchdata.554.